






Competing incommensurate spin fluctuations and magnetic excitations in infinite-layer nickelate superconductors

Christopher Lane ^{1✉}, Ruiqi Zhang ², Bernardo Barbiellini^{3,4}, Robert S. Markiewicz⁴, Arun Bansil ⁴, Jianwei Sun ² & Jian-Xin Zhu ¹

The recently discovered infinite-layer nickelates show great promise in helping to disentangle the various cooperative mechanisms responsible for high-temperature superconductivity. However, lack of antiferromagnetic order in the pristine nickelates presents a challenge for connecting the physics of the cuprates and nickelates. Here, by using a quantum many-body Green's function-based approach to treat the electronic and magnetic structures, we unveil the presence of many two- and three-dimensional magnetic stripe instabilities that are shown to persist across the phase diagram of LaNiO_2 . Our analysis indicates that the magnetic properties of the infinite-layer nickelates are closer to those of the doped cuprates, which host a stripe ground state, rather than the undoped cuprates. The computed longitudinal-spin, transverse-spin, and charge spectra of LaNiO_2 are found to contain an admixture of contributions from localized and itinerant carriers. Theoretically obtained dispersion of magnetic excitations (spin-flip) is found to be in good accord with the results of recent resonant inelastic X-ray scattering experiments. Our study gives insight into the origin of strong magnetic competition in the infinite-layer nickelates and their relationship with the cuprates.

¹Theoretical Division, Los Alamos National Laboratory, Los Alamos, NM 87545, USA. ²Department of Physics & Engineering Physics, Tulane University, New Orleans, LA 70118, USA. ³School of Engineering Science, Lappeenranta-Lahti University of Technology (LUT), Lappeenranta, Finland. ⁴Department of Physics, Northeastern University, Boston, MA 02115, USA. ✉email: laneca@lanl.gov

The common thread linking the family of high-temperature superconductors is that competing interactions involving charge, spin, lattice, and orbital degrees of freedom conspire with electronic correlation effects to produce many complex properties in this materials family¹. The phase diagrams of transition-metal oxides, for example, are astonishingly complex and exhibit unconventional superconducting pairing, pseudogap, and glassy phases, and colossal magnetoresistance in stark contrast to the standard metals^{2–5}. The high- T_c cuprates have been of intense interest, where a wide variety of experiments have reported the presence of competing and intertwined inhomogeneous orders that could contribute to the pairing mechanism^{6–9}. However, deconstructing the mechanism of high- T_c superconductivity and possible contributions involved in the pairing process has remained a challenge. Understanding the electronic and magnetic properties of related materials can provide insight into the mechanism of superconductivity in the cuprates as well as other high- T_c superconductors.

Recently, superconductivity was discovered in doped infinite-layer nickelates¹⁰. The $RNiO_2$ ($R = Nd, Pr, La$) family of compounds is isostructural to the infinite-layer parent cuprate $CaCuO_2$ ¹¹, where the two-dimensional (2D) NiO_2 planes are separated by rare earth spacer layers^{12–14}. Due to the missing apical oxygens in $RNiO_2$, the nickel atoms take a $3d^9$ configuration that is equivalent to Cu^{2+} in the cuprates, thereby strengthening the hypothesis that these two materials' families are electronically analogous^{15,16}.

A number of experimental techniques have been employed to elucidate possible connections between nickel and copper-based superconductivity and the role of competing orders in their phase diagrams. Transport measurements on the nickelates report key departures from the cuprate phenomenology. Specifically, no Mott or antiferromagnetic (AFM) parent phase is observed, with both the underdoped and overdoped nickelates only displaying a weakly insulating state^{13,14,17–25}. The Hall coefficient R_H is found to change sign at optimal doping ($x \sim 0.17$) in all nickelates that have been investigated, signaling the existence and importance of both hole and electron pockets at the Fermi level^{13,14,18,22–27}. X-ray absorption spectroscopy (XAS) and resonant inelastic X-ray scattering (RIXS) experiments find the doped holes to reside on the $Ni-d_{x^2-y^2}$ orbitals, with minor $5d$ electron doping due to $Ni-3d/La-5d$ hybridization^{18,28–30}, suggesting the coexistence of multiple active orbitals at the Fermi level. Despite these differences, the nickelates exhibit signatures of stripe formation and singlets in the ground state, similar to the underdoped cuprates^{14,30–32}.

The magnetic properties of the nickelates differ substantially from those of the cuprates in that the pristine undoped cuprates exhibit commensurate AFM order. In sharp contrast, no long-range AFM order is found in $RNiO_2$ ^{33–36}, despite the existence of robust two-dimensional (2D) AFM spin wave dispersions observed in RIXS^{37,38}. Instead, strong non-local magnetic correlations and weak to intermediate glassy short-range behavior appear to dominate the ground state^{35,39,40}. Moreover, a recent muon spin rotation/relaxation experiment finds the infinite-layer nickelates to be intrinsically magnetic and further provides direct evidence for the coexistence of superconductivity and magnetism, with phase separation only possible on the nano scale⁴¹. This suggests that the magnetic properties of the infinite-layer nickelates are closer to those of the doped cuprates, where inhomogeneities comprise the ground state rather than the undoped cuprates, which present a pristine ordered phase.

Many density functional theory (DFT)^{11,42–48} and DFT + dynamical mean-field theory (DMFT)^{28,39,45,49–51} studies yield a magnetic ground state in the infinite-layer nickelates that are at

odds with the experimental evidence. Dynamical vertex approximation (DVA) and cellular dynamical-mean field theory (CDMFT) calculations³⁹ capture the short-range correlations but do not offer a transparent picture of the instabilities at play. In this connection, a variety of tight-binding models have been invoked^{52–56} to understand the low-energy physics and magnetic instabilities in nickelates. These models, however, are fundamentally limited because the relevant orbitals involved remain unclear.

In this article, we propose that the absence of long-range order in the infinite-layer nickelates originates from a large number of competing symmetry-breaking magnetic instabilities in the pristine phase, which strongly couple at low temperatures as is common in glassy phases of matter. Upon hole doping, these instabilities, originating from the three-dimensionality (3D) of the Fermi surface, pass through a 3D–2D crossover in the magnetic fluctuation spectrum near the onset of the superconducting dome. By using the C-type AFM state as a model system, we simulate the charge and magnetic excitation spectra. By comparing our theoretical spectra to the results from RIXS experiments, we find that the observed dispersion can be reproduced with a renormalization factor of 0.63. Our analysis of the spin-wave spectrum reveals a dominant $Ni-3d_{x^2-y^2}$ contribution along with an admixture of contributions from $Ni-3d_{z^2}$ and $La-4f$ orbitals. Our strongly-constrained-and-appropriately-normed (SCAN) meta-GGA-based results are similar to those obtained using DMFT. A two-band model provides an adequate representation of both charge and magnetic instabilities and excitations.

Results and discussion

Electronic structure and competing fluctuations. Figure 1a shows the interpolated electronic band structure for $LaNiO_2$ in the non-magnetic (NM) phase [Fig. 1b]. In order to conduct an objective analysis of the relevant orbital degrees of freedom at the two-particle level, our atomic orbital model of the NM phase explicitly considers the full set of $Ni-3d$, $La-5d$, and $La-4f$ atomic orbitals. We find the quality of the fit to be quite sensitive to the set of included orbitals. Specifically, due to mixing between the Ni and La states within a 2 eV window of the Fermi level, the removal of even a single $4f$ or $5d$ state results in a poor fit of the $Ni-3d_{x^2-y^2}$ band at the M and A points in the Brillouin zone.

In the lanthanum-based infinite-layer nickelates, three distinct bands cross the Fermi level: one is of nearly pure $Ni-3d_{x^2-y^2}$ character, while the other two are derived from $Ni-3d_{xy/yz}$ and $Ni-3d_{z^2}/La-5d$ orbitals. The latter bands give rise to spherical electron Fermi pockets at the Γ and A symmetry points in the Brillouin zone [Fig. 1c], and may be responsible for the experimentally observed metallic behavior of the resistivity at high temperature^{10,12–14,24,25,35,39}, along with a negative Hall coefficient^{10,13,14,24,25,35}. In contrast, the $Ni-3d_{x^2-y^2}$ band generates a large, slightly warped quasi-2D cylindrical Fermi surface similar to the cuprates. The relatively isolated $Ni-3d_{x^2-y^2}$ state is the result of the oxygen de-intercalation process used to convert $RNiO_3$ to $RNiO_2$, thereby reorganizing the electronic states from that of an octahedral crystal field to a square-planar geometry. The half-filled $Ni-d_{x^2-y^2}$ band closely resembles the corresponding band in the cuprates⁵⁷, except for an enhanced k_z dispersion due to the three-dimensional (3D) nature of the crystal structure. This results in a shift in the position of the van Hove singularity (VHS) from below to infinitesimally above the Fermi level along the k_z direction in the Brillouin zone. Concomitantly, the Fermi surface transitions from being hole-like (open) in the $k_z = 0$ plane to becoming electron-like (closed) in the $k_z = \pi/c$ plane.

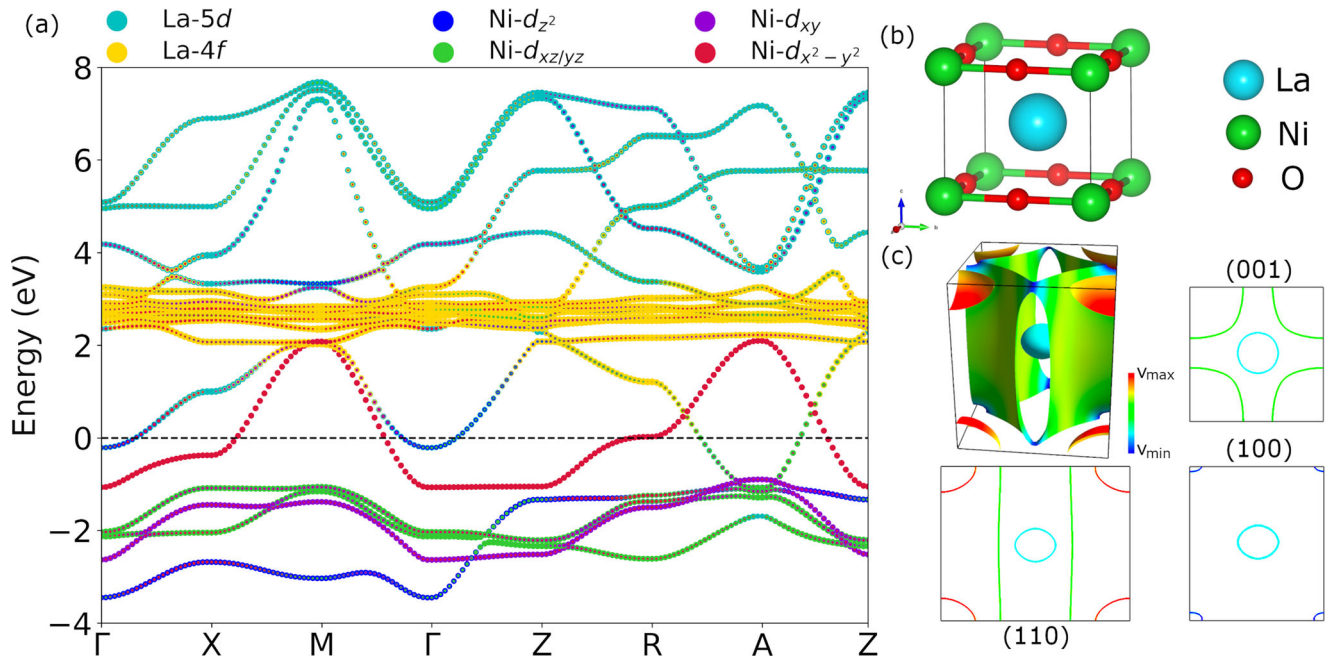


Fig. 1 Crystal and electronic structure of non-magnetic LaNiO₂. **a** Electronic band dispersion in non-magnetic LaNiO₂. The size and color of the dots are proportional to the fractional weight of the various indicated site-resolved orbital projections. **b** Primitive crystal structure of non-magnetic LaNiO₂. **c** Calculated the Fermi surface of LaNiO₂ and its cuts in the (001), (100), and (110) planes. Colors on various Fermi surface sheets indicate the magnitude of the associated Fermi velocities; see colorbar.

A key difference between the parent compounds of the cuprates and nickelates is the lack of long-range magnetic order in the nickelates. Instead, strong AFM correlations and glassy dynamics are observed to dominate throughout the phase diagram of RNiO₂. To gain insight into the landscape of charge and magnetic instabilities in the ground state, we examine the response ($\delta\rho$) of the system to an infinitesimal perturbing source field ($\delta\pi$). The associated response function is given by,

$$\begin{aligned}\chi^{JJ}(1, 2) &= \frac{\delta\rho^J(1)}{\delta\pi^J(2)} \\ &= \chi_0^{JJ}(1, 2) + \chi_0^{IM}(1, 3)v^{ML}(3, 4)\chi^{JJ}(4, 2)\end{aligned}\quad (1)$$

where the orbital indices have been suppressed, the spin indices (I, J, L, M) are given in the Pauli basis, v^{ML} is the generalized electron–electron interaction, and the polarizability is defined as:

$$\begin{aligned}\chi_0^{JJ}(1, 2) &= G(1, 2)G(2, 1^+) \\ &+ G(1, 3)G(4, 1^+)\bar{\Gamma}(3, 4; 9, 10)G(9, 2)G(2^+, 10).\end{aligned}\quad (2)$$

Here, $\bar{\Gamma}$ describes a multiple scattering process involving two quasiparticles with the vertex⁵⁸. Assuming the material exhibits sufficient screening, the vertex correction $\bar{\Gamma}$ can be considered negligible and ignored. Then Eq. (1) can be solved outright, producing a generalized RPA-type matrix equation

$$\begin{aligned}\chi^{MN}(\mathbf{q}, \omega) &= [1 - \chi_0^{MI}(\mathbf{q}, \omega)v^{JK}]^{-1}\chi_0^{KN}(\mathbf{q}, \omega), \\ &= [1 - \bar{F}^{MK}(\mathbf{q}, \omega)]^{-1}\chi_0^{KN}(\mathbf{q}, \omega).\end{aligned}\quad (3)$$

Note that in order to solve for χ^{JJ} , we have introduced the matrix inverse of $[1 - \bar{F}]$. Therefore, extra care must be taken when interpreting the response function. For a system exhibiting an ordered phase, e.g. AFM order, the poles $1 - \bar{F}$ generated in the various spin and orbital channels predict bosonic quasiparticles, such as magnons. In a non-ordered system, if $\chi^{JJ}(\mathbf{q}, \omega = 0) \gg 1$, then the ground state is unstable to a broken-symmetry phase. The specific charge and spin instabilities of the system can be

made transparent by diagonalizing the kernel \bar{F} ,

$$\bar{F} = V(\mathbf{q}, \omega)\Lambda_F(\mathbf{q}, \omega)V^{-1}(\mathbf{q}, \omega)\quad (4)$$

where Λ_F is a diagonal matrix, and V is the eigenvector. Then

$$\chi^{MN}(\mathbf{q}, \omega) = V_{M\alpha}(\mathbf{q}, \omega)[1 - \Lambda_F^\alpha(\mathbf{q}, \omega)]^{-1}V_{\alpha K}^{-1}(\mathbf{q}, \omega)\chi_0^{KN}(\mathbf{q}, \omega).\quad (5)$$

where α enumerates the instability ‘bands.’ Now, as the instability strength $\Lambda_F^\alpha(\mathbf{q}, \omega = 0)$ approaches 1, $\chi^{JJ}(\mathbf{q}, \omega = 0)$ becomes singular, or physically, the ground state becomes unstable to an ordered phase. Additionally, the momentum satisfying $\Lambda_F^{\alpha_{\max}}(\mathbf{Q}, \omega = 0) = 1$, where α_{\max} is the index of the maximum instability band, is the propagating vector \mathbf{Q} of the emerging Stoner instability in the multiorbital spin-dependent system. The character of this instability may then be obtained by analyzing the associated eigenvectors, V .

Figure 2a presents the momentum dependence of the maximum instability $\Lambda_F^0(\mathbf{q}, \omega = 0)$ for pristine LaNiO₂ in the NM phase for various slices along q_z in the Brillouin zone. The overall peak structure in Λ_F^0 follows the folded Fermi surface of the Ni- $3d_{x^2-y^2}$ band, with the main ridges displaying minimal q_z dispersion. The dominant peaks are concentrated around the M – A edge of the Brillouin zone, with weaker satellites along the path connecting the edge and the zone center. The momenta \mathbf{Q}^* of the largest instability (blue and red ‘x’ marks) in each slice is found to evolve along the q_z -axis, taking positions at $(\pi - \delta, \pi, 0)$, $(\pi - \delta, \pi, q_z)$, $(\pi - \delta, \pi - \eta, q_z)$, $(\pi - \xi, \pi - \xi, q_z)$, and (π, π, π) . These momentum points yield nearly degenerate instability strengths, where only 0.0178 separates the critical momenta in the $q_z = 0$ and $q_z = \pi/c$ planes. A similar near degeneracy is found for various in-plane momenta surrounding the M – A edge of the zone [Fig. 2b], with an instability strength difference of 0.0889 and 0.0023 between Q_1 and Q_2 in the Γ and Z planes, respectively. By analyzing the eigenvectors at the various marked \mathbf{Q}^* points, we find magnetic fluctuations to dominate by order of magnitude over the charge sector. Moreover, the transverse and longitudinal

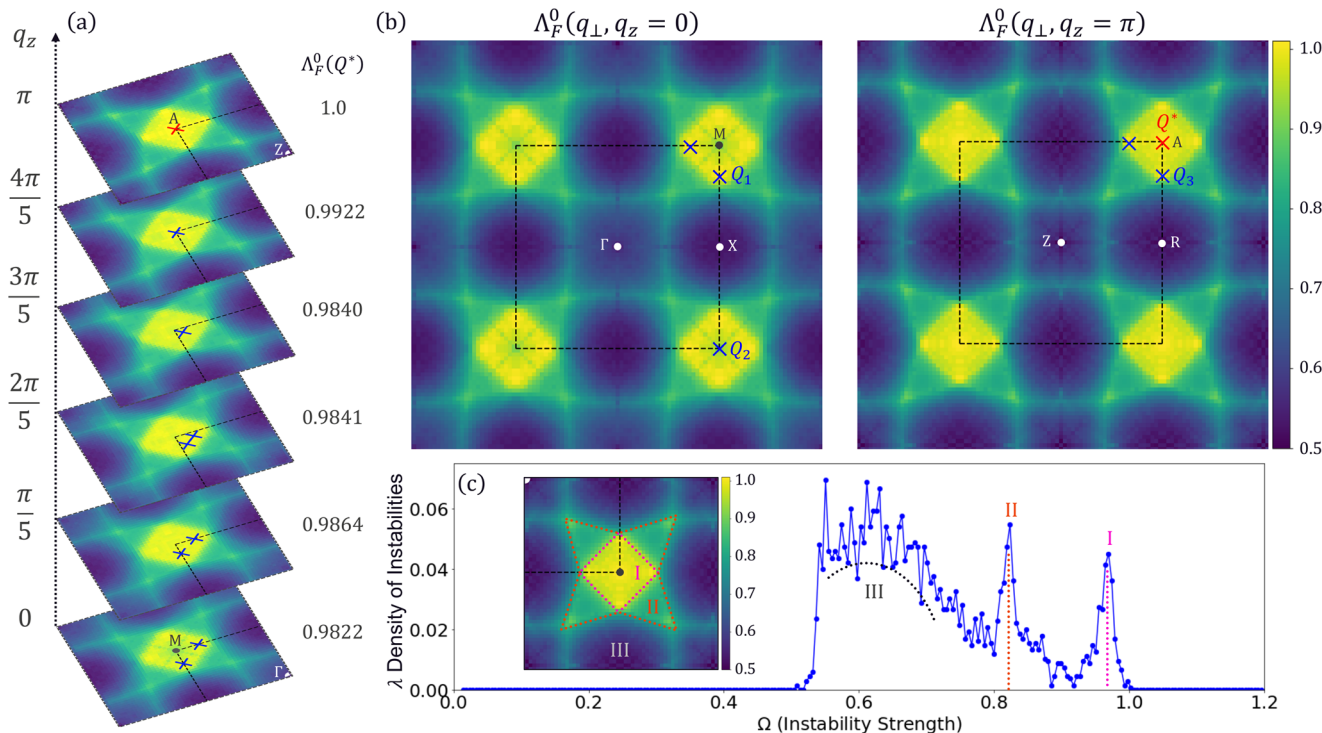


Fig. 2 The spectrum of ordering instabilities in pristine non-magnetic LaNiO₂. Momentum dependence of the largest ordering instability $\Lambda_F^0(\mathbf{q}, \omega = 0)$ for pristine LaNiO₂ in the non-magnetic phase for **a** various slices along q_z , and **b** in the Γ and Z planes of the Brillouin zone. The red and blue “x” marks denote the critical and sub-critical instability momenta \mathbf{Q}^* , respectively. The black dashed line gives the boundary of the Brillouin zone. The color bars indicate the instability strength. **c** Density of instabilities with the two Van Hove-like singularities and the step edge indicated by Roman numerals I, II, and III. The inset in **c** shows the regions of origin in $\Lambda_F^0(\mathbf{q}, \omega = 0)$ of the various marked peaks.

magnetic fluctuations are predominantly composed of intra-orbital Ni-3 $d_{x^2-y^2}$ weight, with additional weak inter-orbital contributions from Ni- $d_{x^2-y^2}$ /Ni- $d_{xy}/xz/yz$ and Ni- $d_{x^2-y^2}$ /La-4 f ($4f_{x(x^2-3y^2)}$ and $4f_{y(3x^2-y^2)}$) hybridization. In contrast, the charge channel is comprised of inter-orbital hybridization between Ni-3 $d_{x^2-y^2}$ and Ni-3 d_{xy} primarily, with smaller overlaps from Ni-3 d_{xz} and Ni-3 d_{yz} orbitals. An additional weak matrix element is found in the Ni-3 $d_{x^2-y^2}$ /La-5 $d_{x^2-y^2}$ channel. These results clearly show that the leading G-type antiferromagnetic instability [$\mathbf{Q}^* = (\pi, \pi, \pi)$] is virtually degenerate with a dense manifold of 2D and 3D incommensurate magnetic stripe orders. This is consistent with total-energy-DFT and DFT+DMFT results yielding a myriad of nearly degenerate magnetic configurations that lower the total energy with respect to the NM phase^{45–48,50,53}.

In Fig. 2a, b, the momentum dependence of the maximum instability is found to be quite flat throughout the Brillouin zone, producing a clear pile-up of various magnetic configurations within an infinitesimally small instability strength. To make this statement more precise and accurately count the total number of competing magnetic configurations, we introduce the density of instabilities $\lambda(\Omega)$, where $\lambda(\Omega)\delta\Omega$ is the number of instabilities in the system whose strengths lie in the range from Ω to $\Omega + \delta\Omega$. That is, $\lambda(\Omega)$ is defined as

$$\lambda(\Omega) = \frac{1}{N_{\mathbf{q}}} \sum_{\alpha \mathbf{q}} \delta(\Lambda_F^\alpha(\mathbf{q}, 0) - \Omega), \quad (6)$$

where Ω is the instability strength and α enumerates the instability eigenvalues defined in Eq. (4). We further emphasize that $\lambda(\Omega)$ contains the instability information for all eigenvalues, not just for the maximum.

Figure 2c shows the density of instabilities for pristine LaNiO₂ in the NM phase, along with an inset illustrating the region of origin of the various key features. The spectrum reveals two clear Van Hove-like singularities, one close to the maximum instability (I) and the other in the body just above 0.8 instability strength (II), along with a large step edge at the bottom of the spectrum (III). Furthermore, by decomposing the density of instabilities into the various band contributions, these peaks are found to originate from dense points in \mathbf{q} -space (Van Hove-like) rather than a clustering of instability “bands”; see Supplementary Note 2 for details. As pointed out by Léon Van Hove⁵⁹ in 1953, the appearance of singular features in the density of states of either electrons or phonons is intimately connected with the topology of the underlying band structure. Here, the presence of these singularities implies the existence of saddle points in the momentum-dependent instability “bands” Λ_F^α . For example, peak I originates from the very subtle change of Λ_F^0 from being a local minimum at $(\pi, \pi, 0)$ to a global maximum at (π, π, π) [Fig. 2a], implying the existence of a critical q_z^* where the concavity changes sign (saddle point). Peak II emerges from the flat plateau between the instability band edges, marked in the inset as the tips of the four-pointed star. The relative placement of the singularities, along with the step-edge III, suggests that the fluctuations in LaNiO₂ are 3D in nature. However, since peak I is in very close proximity to the maximum instability, the system is very close to a 3D–2D transition.

Much like the presence of a Van Hove singularity near the Fermi level can modify and enhance correlated physics of an interacting electron liquid^{60–66}, a similar “Van Hove scenario” arises when a saddle point in the density of instabilities nearly fulfills the Stoner criteria, $\Lambda_F \sim 1$. In the latter case, a large population of charge and magnetic instabilities with different propagating \mathbf{q} -vectors are able to interact and compete with one

another, thus inducing strong correlation corrections to the low-temperature behavior of the system^{67,68}. In line with this scenario, a complimentary study applying DMFT, DFA, and CDMFT to a single-band Hubbard model for NdNiO₂ finds the inclusion of vertex corrections to suppress long-range order, leaving strong short-range correlations to dominate down to very low temperatures³⁹. This study gives credence to the important role that the density of instabilities can play in giving way to strong AFM fluctuations, local magnetism, and a pseudogap-like weakly insulating state.

Figure 3 shows the evolution of the momentum dependence of Λ_F^0 and the corresponding density of instabilities for LaNiO₂ under various hole dopings. As hole carriers are added, the Ni-3d_{x²-y²} Fermi surface sheet expands in volume, gradually reducing and eliminating the electron-like Fermi surface in the $k_z = \pi/c$ plane. Consequently, the areas of regions I and II in Λ_F^0 grow with increased hole concentration, as shown in Fig. 2c. Moreover, the concavity of Λ_F^0 at (π, π, π) goes from negative to positive around 10% hole doping, as illustrated by the critical momenta (red ‘x’ marks), which change location from (π, π, π) to $(\pi - \delta, \pi - \eta, \pi)$. This process is reflected in the density of instabilities where peak I transitions from a saddle point ($x = 0.0$) to a step edge ($x = 0.30$). The Van Hove-like singularity thus precipitates an effective dimensionality reduction of the fluctuations from 3D to 2D. Curiously, this transition appears just before the sign change in the Hall coefficient at the start of the superconducting dome²⁴. Finally, at $x = 0.4$, the leading edge of the density-of-instabilities softens, exhibiting the presence of a small number of instabilities and suggesting a severe reduction in the competition between the various magnetic configurations.

The persistence of the peak I at or near the maximum instability edge for both the underdoped and overdoped regimes suggests the preservation of strong competition between the magnetic states, despite the systematic reduction in the fluctuation strength with doping. The 3D to quasi-2D transition in the nature of the fluctuations just before optimal doping makes LaNiO₂ distinct from the cuprates, which display predominantly 2D fluctuations for all hole dopings. Furthermore, this suggests that 2D magnetic fluctuations, in particular, are important for Cooper pairing, with optimal T_c arising from the delicate balance between the dimensionality and strength of the fluctuations. In this connection, recent magnetotransport measurements find superconductivity to be quasi-two-dimensional in the infinite-layer nickelates⁶⁹.

Spin excitation spectra. So far, we have examined the manifold of possible magnetic states that may emerge from the non-magnetic state of pristine and doped LaNiO₂. We now turn to examine the charge and spin excitations that occur within the magnetic state to gain insight into the measured magnetic excitation spectrum^{38,70}.

Figure 4a presents the band structure of LaNiO₂ in the C-AFM phase. Our model of the C-AFM phase explicitly considers the full set of Ni-3d, La-5d_{z²}, La-5d_{xy}, La-4f_{z³}, and La-4f_{x(x²-3y²)} orbitals. Reducing the orbital projections further resulted in a poor fit. The AFM state stabilizes in the Ni-3d_{x²-y²} band with a gap of approximately 2 eV that opens up around the Fermi energy of the NM system. The partially filled Ni-3d_{xy/yz} and Ni-3d_{z²} bands remain pinned to the Fermi level, with the Ni-3d_{z²} state becoming flat in the Z plane. Unlike the parent cuprate compounds, itinerant excitations are expected in addition to those of the local magnetic moments.

The charge $-\text{Im}\chi^{00}$, longitudinal-spin $-\text{Im}\chi^{zz}$ and transverse-spin (spin-flip) $-\text{Im}\chi^{+-}$ excitation spectra are obtained from the corresponding components of the dynamical response χ^{IJ} [Eq. (3)]

applied to the magnetic ground state. It is also useful to define the *total spectrum* $\sum_{\nu\nu',\mu\mu'}\chi_{\nu\nu',\mu\mu'}^{IJ}$ where all four indices are integrated out and the *maximum spectra tensor* $\max_{\mathbf{q},\omega}\left\{\left|\chi_{\nu\nu',\mu\mu'}^{IJ}(\mathbf{q},\omega)\right|\right\}$ for the various charge (spin) components I, J . Finally, we introduce a scaled unit of energy $\bar{\omega} = \varepsilon_r \cdot \omega$ to evaluate the excitation energy under renormalization effects, which are common when itinerant carriers are present in an antiferromagnet⁷¹. Moreover, ε_r is inversely proportional to the quasiparticle renormalization factor Z ⁷². Comparing our spectrum to the reported RIXS spectra^{38,70}, we find a renormalization ε_r value of 0.63 ($Z = 1.58$), which suggests LaNiO₂ to be an intermediately coupled material. Interestingly, this renormalization also corresponds to ~26% hole-doped La₂CuO₄⁷³ and optimally doped BaFe₂As₂⁷⁴. We note that the dipole matrix elements of the RIXS measurement process may also be included to capture polarization effects⁷⁵.

Figure 4b shows the total transverse-spin excitation spectrum along the various high-symmetry lines in the NM Brillouin zone, with the experimental data overlaid^{38,70}. Highly dispersive magnetic excitations are found following the spin-1/2 AFM magnons on a square lattice. Specifically, they disperse strongly with maxima at X and M/2, and linearly soften toward the AFM ordering wave vector at M in very good accord with the experimental spectra. Our theoretical excitations display a gap in the Γ plane compared to those in the plane through Z. This behavior is typical of infinite-layer perovskites, such as CaCuO₂⁷⁶, where a pronounced in- and out-of-plane exchange coupling anisotropy can gap out magnetic excitations. By inspection of our electronic band’s structure, this gap can be attributed to the very small electron pockets at the Fermi level in the Γ -plane compared to those in the Z-plane. Additional small anisotropies within the xy -plane are also noticed.

Figure 4c, d presents the total longitudinal-spin spectrum and the charge spectrum, respectively, along the various high-symmetry lines in the NM Brillouin zone. Both spectra are very similar, exhibiting a broad continuum of excitations. The excitation spectrum is amplified in the $q_z = \pi$ plane as a consequence of the flat Ni-3d_{z²} band at the Fermi level. The incorporation of spin-orbit coupling effects in the electronic structure gives rise to significant mixing between the transverse-spin and charge sectors, as indicated by the non-zero χ^{0-} and χ^{0+} susceptibility components, see Sec. S3 of Supplementary Note 3 for details, and yield a “shadow” of the spin-flip excitations in the Γ plane and along Γ -Z in χ^{00} .

Figure 5a displays the maximum spectra tensor of the transverse-spin susceptibility as a heat map with the ν, μ (ν', μ') indices unrolled along the horizontal (vertical) axis. To help identify key atomic-site orbital components and asymmetries in the tensor, the left (right) distribution curve—given by the sum of each row (column)—is presented in the right (top) sub-panel. The right and left distribution curves can be thought of as being similar to the spin-density ($S_{\mu\nu}$) amplitude, and their overlap $\langle S_{\mu\nu}^+, S_{\mu'\nu'}^- \rangle$ is akin to the heat map.

Since the maximum-spectra-tensor heat map is symmetric about the anti-diagonal, the left and right distribution curves are equivalent. The distribution curves are quite sparse, exhibiting only a few prominent peaks in the $(\text{Ni-3d}_{x^2-y^2}, \text{Ni-3d}_{x^2-y^2})$ channel, with smaller peaks present in the $(\text{Ni-3d}_{z^2}, \text{Ni-3d}_{z^2})$ and $(\text{La-4f}_{x(x^2-3y^2)}, \text{Ni-3d}_{x^2-y^2})$ components. In the heat map, these peaks appear as ‘hot’ horizontal and vertical lines, with maxima occurring at their intersection points (white arrows). These maxima identify the key atomic-site orbital components of the transverse-spin susceptibility. Specifically, our orbital analysis reveals that the magnetic excitations are dominated by Ni-3d_{x²-y²} $\chi_{\mu\mu,\mu\mu}^{+-}$ character, suggesting that the Ni-3d_{x²-y²} orbital plays an important role in the local magnetic moment. Ab initio

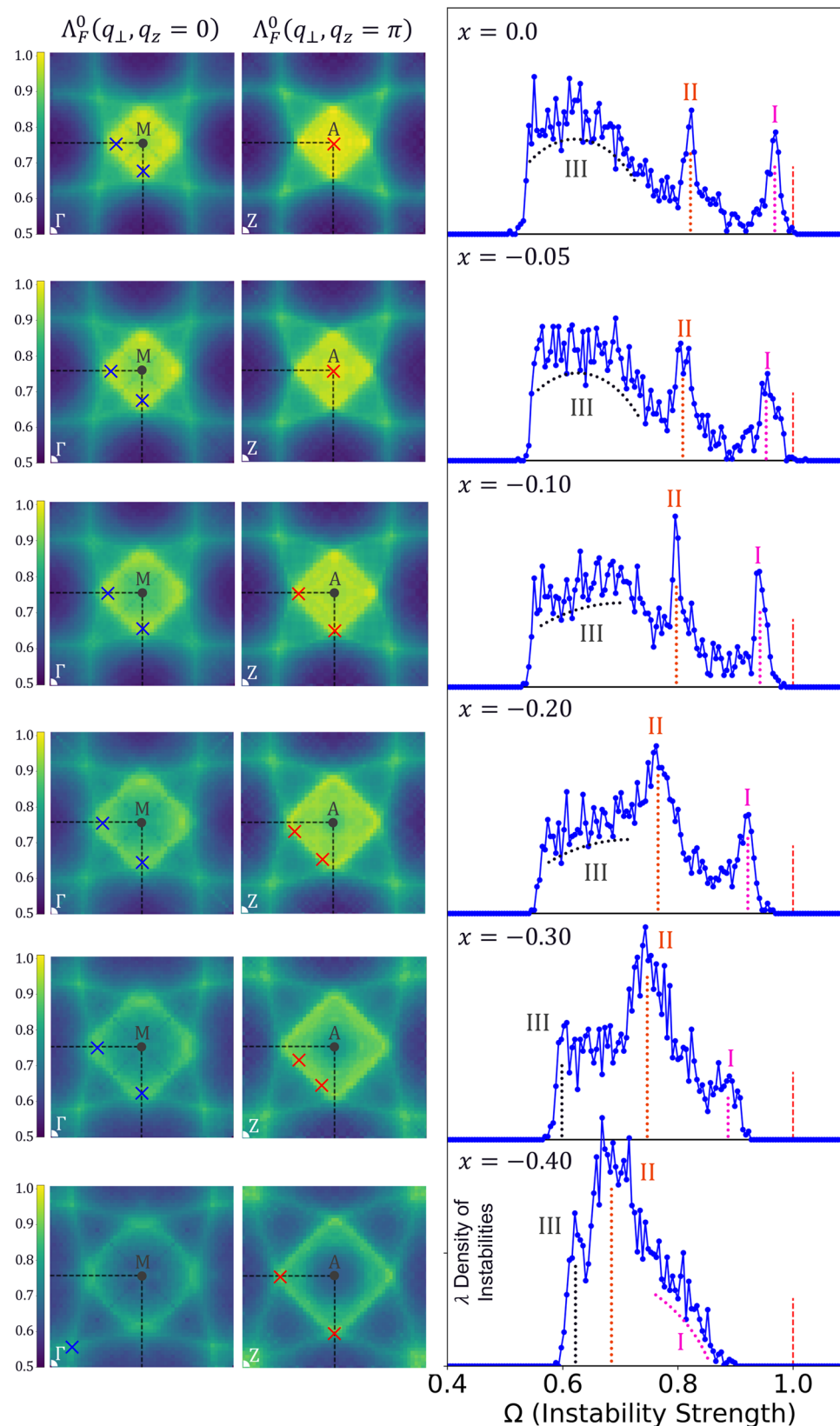


Fig. 3 The evolution of ordering instabilities with hole concentration in non-magnetic LaNiO₂. Momentum dependence of the maximum instability $\Lambda_F^0(\mathbf{q}, \omega = 0)$ in the Γ and Z planes of the Brillouin zone, along with the corresponding density of instabilities of LaNiO₂ in the non-magnetic phase for various hole dopings. Red and blue "x" marks identify the critical and sub-critical instability momenta \mathbf{Q}^* , respectively. The black dashed line denotes the boundary of the Brillouin zone. The color bars indicate the instability strength. The two Van Hove singularities and the step-edge are indicated by Roman numerals I, II, and III.

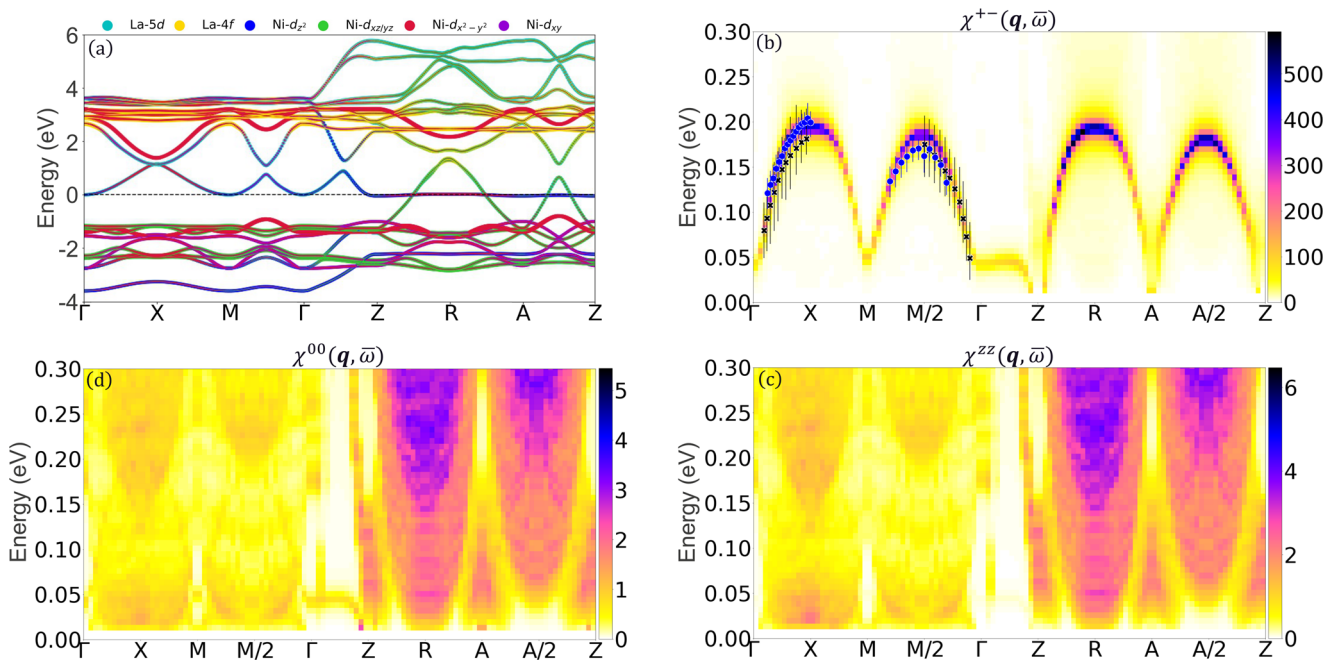


Fig. 4 Ground state electronic structure and excitation spectrum of C-type antiferromagnetic LaNiO₂. **a** Electronic band dispersion for LaNiO₂ in the C-type antiferromagnetic phase. The size of the dots is proportional to the fractional weight of the various indicated site-resolved orbital projections. The total **b** spin-transverse, **c** spin-longitudinal, and **d** charge excitation spectrum along the various high-symmetry lines in the non-magnetic Brillouin zone. The corresponding experimental transverse-spin data (blue circles⁷⁰ and red crosses³⁸) are overlaid in panel **(b)**. The error bars were estimated by combining the uncertainty of zero-energy-loss position, high-energy background, and the standard deviation of the fits, see⁷⁰ and³⁸. The color bars indicate the excitation spectrum intensity.

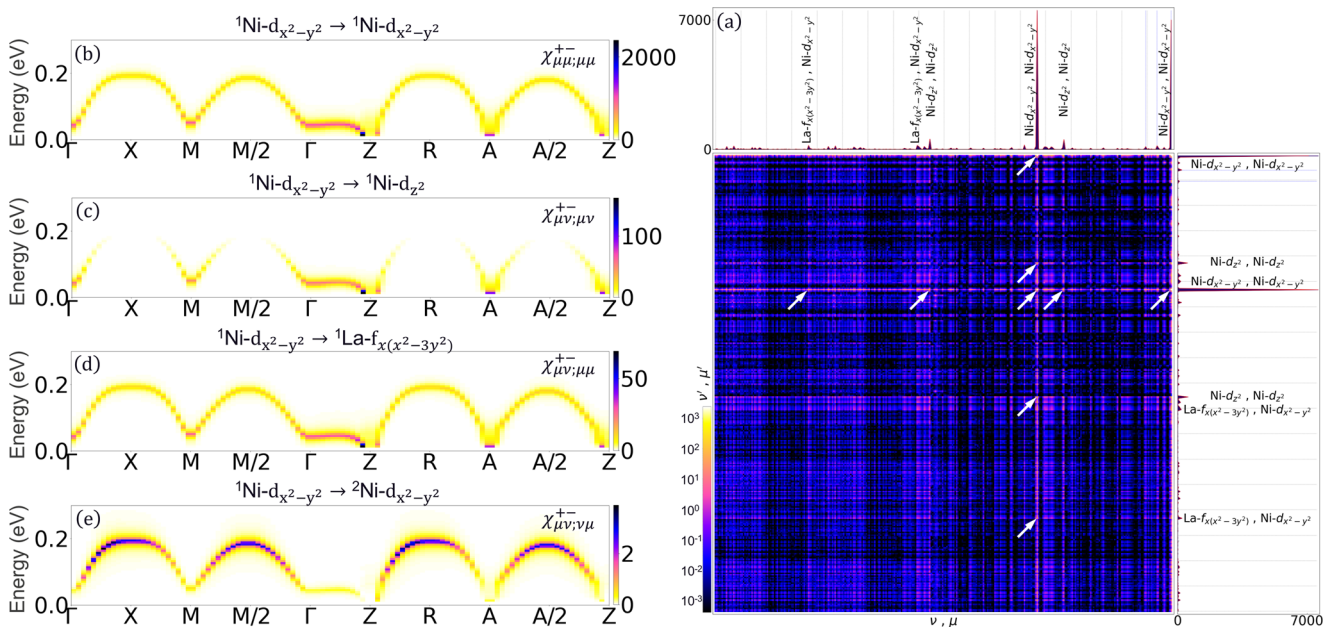


Fig. 5 Orbitally resolved transverse-spin excitation spectrum of C-type antiferromagnetic LaNiO₂. **a** Heat map of the transverse-spin susceptibility maximum spectra tensor, with corresponding distribution curves. The transverse spin excitation spectrum for **b** intra-orbital Ni-3d_{x²-y²}, **c** intra-site ¹Ni - 3d_{x²-y²} → ¹Ni - 3d_{z²}, **d** ¹Ni - 3d_{x²-y²} → ¹La - 4f_{x(x²-3y²)}}, and **e** inter-site ¹Ni - 3d_{x²-y²} → ²Ni - 3d_{x²-y²} excitations along the various high-symmetry lines in the non-magnetic Brillouin zone. The color bars indicate the excitation spectrum intensity.

calculations show a similar trend where the Ni-3d_{x²-y²} contributes 75% to the total Ni magnetic moment⁴⁸. The corresponding excitation spectrum of the Ni-3d_{x²-y²} component is given in Fig. 5b.

The sub-dominant spin-excitation components arise as off-diagonal components of the heat map that mix Ni-3d_{x²-y²} with other Ni-3d and Ni-4f states. The intra-site χ_{μν;μν}⁺⁻ term capturing ¹Ni - 3d_{x²-y²} → ¹Ni - 3d_{z²} transitions [Fig. 5c] contribute to the

low-energy part of the total spectrum near the center $\Gamma(Z)$ and corner $M(A)$ of the Brillouin zone. In contrast, long-range interstate $\chi_{\mu\nu;\nu\mu}^{+-}$ ${}^1\text{Ni} - 3d_{x^2-y^2} \rightarrow {}^2\text{Ni} - 3d_{x^2-y^2}$ excitations [Fig. 5e] have the greatest amplitude around 0.20 meV/ ϵ_r centered around $X(R)$ and $M/2(A/2)$. The mixed term $\chi_{\mu\nu;\nu\mu}^{+-}$ captures the coupling of a local ${}^1\text{Ni} - 3d_{x^2-y^2}$ excitation to a non-local ${}^1\text{Ni} - 3d_{x^2-y^2} \rightarrow {}^1\text{Ni} - 4f_{x(x^2-3y^2)}$ transition [Fig. 5d]. This term indicates that non-trivial Ni–La hybridization can play a role (order of 2%) in influencing the magnon dispersion throughout the Brillouin zone and could contribute to the long-range behavior of the Heisenberg exchange parameters³⁷. This is in contrast to the cuprates, where spin excitations are highly localized on the copper atoms⁷⁷.

Comparison with other approaches. The discovery of a new class of superconductors not only brings forth new insights into the microscopic pairing mechanisms involved but it also provides a new data point for benchmarking and comparing various theoretical approaches toward superconductivity. Much of the existing theoretical analysis of the infinite-layer nickelates has been based on the standard DFT and DFT + DMFT frameworks. In this connection, it is useful to compare and contrast our results based on the more recently constructed SCAN meta-GGA density functional, which has been shown to yield a systematic improvement in capturing the properties of wide classes of materials^{78,79}, with electronic structures of the infinite-layer nickelates available in the literature.

In the NM state, SCAN and the local density approximation (LDA)¹⁶—used to initialize the DMFT—yield very similar results in a $\pm 2\text{eV}$ energy window around the Fermi energy, with small differences appearing in band dispersions outside this energy window due to La–Ni ($\text{Ni}-t_{2g}$ and $\text{Ni}-3d_{z^2}$) hybridization. LDA and SCAN are thus expected to yield the same instabilities. When the spin degrees of freedom are allowed to relax in SCAN, however, a C-AFM ground state is obtained, whereas when spin-polarized DMFT corrections are applied, a G-AFM ground state is found with a C-AFM order only $\sim 6\text{meV}$ higher in energy⁸⁰. This small difference in total energies can be explained by the additional lattice relaxations involved in the SCAN calculations. The DMFT instabilities are similar to those found via our RPA instability analysis. Both SCAN and DFT + DMFT⁸⁰ (spin-polarized) find the $\text{Ni}-3d_{z^2}$ states pushed to the Fermi level forming a flat band, as was also reported using DFT + U⁸¹. The spin-polarized (C-AFM) SCAN electronic dispersions are also similar to the PM DFT + DMFT and DFT + self-interaction corrected DMFT (sicDMFT) results⁸². Specifically, the atomically-resolved band dispersions from SCAN are comparable to the $\text{Ni}-3d_{t_{2g}}$ states of DFT + DMFT and the $\text{Ni}-3d_{x^2-y^2}$ and flat $\text{Ni}-3d_{z^2}$ states of DFT + sicDMFT, where $\text{Ni}-3d_{x^2-y^2}$ bands are completely absent at the Fermi level. This suggests that SCAN is adequately capturing the spin correlations. Further studies involving larger crystallographic unit cells to reveal the emergence of short-range spin-symmetry breaking would be interesting⁸³.

We turn next to compare the transverse-spin response within SCAN and DMFT. The PM DFT + sicDMFT spin response spectra⁸⁴ appear to capture the linear softening of the magnon dispersion near Γ but fail to display the high-energy features at X and $M/2$, which are seen clearly in the experimental dispersion. The SCAN-based results match the RIXS curves over the full Brillouin zone when a renormalization factor is applied, as is typical for doped antiferromagnets. This is consistent with the reports of short-range magnetic dynamics over pure local moment fluctuations in LaNiO_2 ³⁹. Since both approaches use the same RPA framework to obtain the spin response, it will be

interesting to evaluate corrections to the ground state using CDMFT or SCAN based on supercells involving large special quasirandom structures (SQS)⁸⁵ to better capture the short-range correlations.

Low-energy models of the electronic structure are useful for disentangling the relationship between physical phenomena and the local chemistry, and indeed many such models have been invoked for the infinite-layer nickelates. Since we employ a multiorbital model spanning $\text{Ni}-3d$, $\text{La}-5d$, and $\text{La}-4f$ orbitals, we are in a position to help identify a minimal set of orbitals necessary to reproduce the fluctuation instabilities and excitations. Our analysis of the NM phase shows that a simple model composed of a single $\text{Ni}-3d_{x^2-y^2}$ orbital can capture the magnetic fluctuations, consistent with the observations of Kitatani et al.^{54,86}. To reproduce both the charge and magnetic fluctuations, however, a minimum of two orbitals is required. The minimal Hamiltonian proposed by Hu et al.⁸⁷ using $\text{Ni}-3d_{x^2-y^2}$ and $\text{Ni}-3d_{xy}$ states is in good accord with our work, whereas the proposed Hamiltonians using $\text{Ni}-3d_{z^2}$ ^{45,88–90}, $\text{Ni}-s$ ⁹¹, or $\text{La}-5d$ ^{29,92} states instead of $\text{Ni}-3d_{xy}$ are not well-suited for modeling the NM state. However, if one wishes to self-consistently include magnetic correlation effects into the model—a prerequisite for capturing the magnetic excitation spectrum—, two-band Hamiltonians using $\text{Ni}-3d_{z^2}$ states should be considered instead of those employing $\text{Ni}-3d_{xy}$ orbitals in order to reproduce the partially occupied flat band at the Fermi level. Finally, if capturing the subtle effects arising from non-trivial Ni–rare earth hybridization are important, three-^{56,93–95} and four-band^{53,96} models provide a more faithful description.

Conclusions

Our study demonstrates that LaNiO_2 supports myriad competing, incommensurate spin fluctuations and magnetic excitations that are spread over multiple atomic sites. The reduction in the dimensionality of the magnetic fluctuations (3D to 2D) is found to coincide with the emergence of superconductivity. With further hole doping, fluctuations weaken, and superconductivity disappears, suggesting a tradeoff between the dimensionality and the strength of magnetic fluctuations in controlling the value of T_c . This behavior is similar to that of the doped cuprates where 2D inhomogeneous magnetic stripes are manifest already in the ground state⁹⁷. Our study gives insight into the nature of strong correlations in nickelates and provides a pathway for investigating complex correlated materials more generally.

Methods

First-principles calculations. Ab initio calculations were carried out by using the pseudopotential projector-augmented wave method⁹⁸ implemented in the Vienna ab initio simulation package (VASP)^{99,100} with an energy cutoff of 520 eV for the plane-wave basis set. Exchange-correlation effects were treated by using the strongly-constrained-and-appropriately-normed (SCAN) meta-GGA density functional¹⁰¹. A $15 \times 15 \times 17$ Γ -centered k -point mesh was used to sample the Brillouin zone. Spin-orbit coupling effects were included self-consistently. We used the experimental low-temperature P4/mmm crystal structure to initialize our computations³⁴. All atomic sites in the NM and C-AFM unit cells, along with the cell dimensions, were relaxed using a conjugate gradient algorithm to minimize the energy with an atomic force tolerance of 0.01 eV/Å. A total energy tolerance of 10^{-5} eV was used to determine the self-consistent charge density.

Tight-binding Hamiltonian details. The many-body theory calculations of the spin-orbital fluctuations and magnetic excitations were performed by employing a real-space tight-binding model Hamiltonian, which was obtained by using the VASP2WANNIER90¹⁰² interface. For LaNiO_2 , the full manifold of $\text{Ni}-3d$, $\text{La}-5d$, and $\text{La}-4f$ states (a total of 17 orbitals) was included in generating the orbital projections, whereas in the C-AFM phase the d_{z^2} , d_{xy} , f_{z^3} , and $f_{x(x^2-3y^2)}$ were retained on the La sites (a total of 18 orbitals). We considered models employing a smaller number of basis functions for both the NM and C-AFM phase, but the resulting fits were quite poor. The Fourier transform convention $H_{ij}(\mathbf{k}) = \sum_{\mathbf{R}} e^{i\mathbf{k}\cdot\mathbf{R}} H_{ij}(\mathbf{R})$, is used throughout this work.

Response function calculations. In the NM state, a $51 \times 51 \times 51\Gamma$ -centered k -mesh was used to evaluate the response functions in the Brillouin zone. Only the 4 bands at the Fermi level were used in the summation over the bands in the Lindhard susceptibility. In the C-AFM phase, a $23 \times 23 \times 23\Gamma$ -centered k -mesh was employed to sample the Brillouin zone, along with $101(2001)\omega$ -mesh(X -mesh) energy points spanning 0–1 eV (–10 eV to 10 eV). See Supplementary Note 1 for a detailed definition of the ω and X meshes used in the “binning” method^{103–105}. All the bands were used in the eigenvalue integration for the C-AFM phase. A small broadening of 0.01 eV was used to simulate experimental conditions. Since our susceptibility code allows for finite temperatures, a very low value of the temperature of $T = 0.001$ K was used to mimic the DFT conditions and approximate a Heaviside step function. Coulomb interactions were included on the Ni- d orbitals and assumed to be rotationally symmetric, i.e. fulfilling the constraint $U' = U - 2J$ and $J = J^{58}$. The maximum instability $\Lambda_{\vec{k}}^0(\mathbf{Q}^*)$ was found to equal 1 for U , U' , and J values of 1.22 eV, 0.732 eV, and 0.244 eV, respectively. Our results are insensitive to changes in J and show the dominance of Ni- $d_{x^2-y^2}$ orbital at the Fermi level. We also find negligible effect of including U , U' , and J Coulomb parameters on La- $5d$ states. The values of U , U' , and J used were 3.675, 2.109, 0.782 eV, respectively, to simulate the magnon dispersion, where the ratio $U/J = 5$ was taken from SCAN ground state calculations⁴⁸.

Data availability

All data supporting the findings of this study are available from the corresponding author upon a reasonable request.

Code availability

The code used to calculate the spin-orbital fluctuations and magnetic excitations is currently in the process of becoming open source. Requests about the code should be made to the corresponding author.

Received: 8 September 2022; Accepted: 20 April 2023;

Published online: 03 May 2023

References

- Dagotto, E. Complexity in strongly correlated electronic systems. *Science* **309**, 257–262 (2005).
- Keimer, B., Kivelson, S. A., Norman, M. R., Uchida, S. & Zaanen, J. From quantum matter to high-temperature superconductivity in copper oxides. *Nature* **518**, 179–186 (2015).
- Dagotto, E. *Nanoscale Phase Separation and Colossal Magnetoresistance: The Physics Of Manganites And Related Compounds* (Springer Science & Business Media, 2003).
- Platzman, P. M. & Wolff, P. A. *Waves and interactions in solid state plasmas*, vol. 13 (Academic Press New York, 1973).
- Sobota, J. A., He, Y. & Shen, Z.-X. Angle-resolved photoemission studies of quantum materials. *Rev. Mod. Phys.* **93**, 025006 (2021).
- Fradkin, E., Kivelson, S. A. & Tranquada, J. M. Colloquium: theory of intertwined orders in high temperature superconductors. *Rev. Mod. Phys.* **87**, 457 (2015).
- He, Y. et al. Rapid change of superconductivity and electron-phonon coupling through critical doping in Bi-2212. *Science* **362**, 62–65 (2018).
- Li, H. et al. Coherent organization of electronic correlations as a mechanism to enhance and stabilize high- T_C cuprate superconductivity. *Nat. Commun.* **9**, 1–9 (2018).
- Jiang, H.-C. & Kivelson, S. A. Stripe order enhanced superconductivity in the Hubbard model. *Proc. Natl Acad. Sci.* **119**, e2109406119 (2022).
- Li, D. et al. Superconductivity in an infinite-layer nickelate. *Nature* **572**, 624–627 (2019).
- Botana, A. S. & Norman, M. R. Similarities and differences between LaNiO_2 and CaCuO_2 and implications for superconductivity. *Phys. Rev. X* **10**, 011024 (2020).
- Osada, M. et al. A superconducting praseodymium nickelate with infinite layer structure. *Nano Lett.* **20**, 5735–5740 (2020).
- Osada, M. et al. Nickelate superconductivity without rare-earth magnetism: $(\text{La,Sr})\text{NiO}_2$. *Adv. Mater.* **33**, 2104083 (2021).
- Zeng, S. et al. Phase diagram and superconducting dome of infinite-layer $\text{Nd}_{1-x}\text{Sr}_x\text{NiO}_2$ thin films. *Phys. Rev. Lett.* **125**, 147003 (2020).
- Anisimov, V., Bukhvalov, D. & Rice, T. Electronic structure of possible nickelate analogs to the cuprates. *Phys. Rev. B* **59**, 7901 (1999).
- Lee, K.-W. & Pickett, W. Infinite-layer LaNiO_2 : Ni^{1+} is not Cu^{2+} . *Phys. Rev. B* **70**, 165109 (2004).
- Goode, B. H. et al. Doping evolution of the Mott–Hubbard landscape in infinite-layer nickelates. *Proc. Natl Acad. Sci. USA* **118**, e2007683118 (2021).
- Gu, Q. & Wen, H. Superconductivity in nickel based 112 systems. *The Innovation* **3**, 100202 (2022).
- Hsu, Y.-T. et al. Correlated insulating behavior in infinite-layer nickelates. *Front. Phys.* **10**, 846639 (2022).
- Chow, L. E. & Ariando, A. Infinite-layer nickelate superconductors: a current experimental perspective of the crystal and electronic structures. *Front. Phys.* **10**, 20 (2022).
- Nomura, Y. & Arita, R. Superconductivity in infinite-layer nickelates. *Rep. Prog. Phys.* **85**, 052501 (2022).
- Li, D. et al. Superconducting dome in $\text{Nd}_{1-x}\text{Sr}_x\text{NiO}_2$ infinite layer films. *Phys. Rev. Lett.* **125**, 027001 (2020).
- Osada, M., Wang, B. Y., Lee, K., Li, D. & Hwang, H. Y. Phase diagram of infinite layer praseodymium nickelate $\text{Pr}_{1-x}\text{Sr}_x\text{NiO}_2$ thin films. *Phys. Rev. Mater.* **4**, 121801 (2020).
- Zeng, S. et al. Superconductivity in infinite-layer nickelate $\text{La}_{1-x}\text{Ca}_x\text{NiO}_2$ thin films. *Sci. Adv.* **8**, eabl9927 (2022).
- Lee, K. et al. Character of the normal state of the nickelate superconductors. Preprint at arXiv <https://doi.org/10.48550/arXiv.2203.02580> (2022).
- Mitchell, J. A. nickelate renaissance. *Front. Phys.* **9**, 813483 (2021).
- Chen, Z. et al. Electronic structure of superconducting nickelates probed by resonant photoemission spectroscopy. *Matter* **5**, 1806–1815 (2022).
- Higashi, K., Winder, M., Kuneš, J. & Hariki, A. Core-level X-ray spectroscopy of infinite-layer nickelate: LDA+ DMFT study. *Phys. Rev. X* **11**, 041009 (2021).
- Hepting, M. et al. Electronic structure of the parent compound of superconducting infinite-layer nickelates. *Nat. Mater.* **19**, 381–385 (2020).
- Rossi, M. et al. Orbital and spin character of doped carriers in infinite-layer nickelates. *Phys. Rev. B* **104**, L220505 (2021).
- Rossi, M. et al. A broken translational symmetry state in an infinite-layer nickelate. *Nat. Phys.* **18**, 869–873 (2022).
- Tam, C. C. et al. Charge density waves in infinite-layer NdNiO_2 nickelates. *Nat. Mater.* **21**, 1116–1120 (2022).
- Hayward, M., Green, M., Rosseinsky, M. & Sloan, J. Sodium hydride as a powerful reducing agent for topotactic oxide deintercalation: synthesis and characterization of the nickel (i) oxide LaNiO_2 . *J. Am. Chem. Soc.* **121**, 8843–8854 (1999).
- Hayward, M. & Rosseinsky, M. Synthesis of the infinite layer Ni (i) phase NdNiO_{2+x} by low temperature reduction of NdNiO_3 with sodium hydride. *Solid State Sci.* **5**, 839–850 (2003).
- Ikeda, A., Krockenberger, Y., Irie, H., Naito, M. & Yamamoto, H. Direct observation of infinite NiO_2 planes in lanio_2 films. *Appl. Phys. Express* **9**, 061101 (2016).
- Crespin, M., Levitz, P. & Gataineau, L. Reduced forms of LaNiO_3 perovskite. Part 1. Evidence for new phases: $\text{La}_2\text{Ni}_2\text{O}_5$ and LaNiO_2 . *J. Chem. Soc. Faraday Trans. 2 Mol. Chem. Phys.* **79**, 1181–1194 (1983).
- Lu, H. et al. Magnetic excitations in infinite-layer nickelates. *Science* **373**, 213–216 (2021).
- Krieger, G. et al. Charge and spin order dichotomy in ndnio_2 driven by the capping layer. *Phys. Rev. Lett.* **129**, 027002 (2022).
- Ortiz, R. et al. Magnetic correlations in infinite-layer nickelates: an experimental and theoretical multimethod study. *Phys. Rev. Res.* **4**, 023093 (2022).
- Lin, H. et al. Universal spin-glass behaviour in bulk LaNiO_2 , PrNiO_2 and NdNiO_2 . *N. J. Phys.* **24**, 013022 (2022).
- Fowlie, J. et al. Intrinsic magnetism in superconducting infinite-layer nickelates. *Nat. Phys.* **18**, 1043–1047 (2022).
- Botana, A. S., Lee, K.-W., Norman, M. R., Pardo, V. & Pickett, W. E. Low valence nickelates: launching the nickel age of superconductivity. *Front. Phys.* **9**, 813532 (2022).
- Kapeghian, J. & Botana, A. S. Electronic structure and magnetism in infinite-layer nickelates RNiO_2 ($R = \text{La-Lu}$). *Phys. Rev. B* **102**, 205130 (2020).
- LaBollita, H. & Botana, A. S. Electronic structure and magnetic properties of higher-order layered nickelates: $\text{La}_{n+1}\text{Ni}_n\text{O}_{2n+2}$ ($n = 4-6$). *Phys. Rev. B* **104**, 035148 (2021).
- Wan, X., Ivanov, V., Resta, G., Leonov, I. & Savrasov, S. Y. Exchange interactions and sensitivity of the ni two-hole spin state to Hund's coupling in doped ndnio_2 . *Phys. Rev. B* **103**, 075123 (2021).
- Liu, Z., Ren, Z., Zhu, W., Wang, Z. & Yang, J. Electronic and magnetic structure of infinite-layer NdNiO_2 : trace of antiferromagnetic metal. *npj Quantum Mater.* **5**, 1–8 (2020).
- Jung, M.-C., LaBollita, H., Pardo, V. & Botana, A. S. Antiferromagnetic insulating state in layered nickelates at half filling. *Sci. Rep.* **12**, 17864 (2022).
- Zhang, R. et al. Magnetic and f -electron effects in lanio_2 and ndnio_2 nickelates with cuprate-like $3d_{x^2-y^2}$ band. *Commun. Phys.* **4**, 1–12 (2021).

49. Wang, Y., Kang, C.-J., Miao, H. & Kotliar, G. Hund's metal physics: from SrNiO₂ to LaNiO₂. *Phys. Rev. B* **102**, 161118 (2020).
50. Lechermann, F. Doping-dependent character and possible magnetic ordering of NdNiO₂. *Phys. Rev. Mater.* **5**, 044803 (2021).
51. Gu, Y., Zhu, S., Wang, X., Hu, J. & Chen, H. A substantial hybridization between correlated Ni-d orbital and itinerant electrons in infinite-layer nickelates. *Commun. Phys.* **3**, 1–9 (2020).
52. Sakakibara, H. et al. Model construction and a possibility of cupratelike pairing in a new d⁹ nickelate superconductor (Nd,Sr)NiO₂. *Phys. Rev. Lett.* **125**, 077003 (2020).
53. Gu, Y., Zhu, S., Wang, X., Hu, J. & Chen, H. A substantial hybridization between correlated Ni-d orbital and itinerant electrons in infinite-layer nickelates. *Commun. Phys.* **3**, 84 (2020).
54. Kitatani, M. et al. Nickelate superconductors—a renaissance of the one-band Hubbard model. *npj Quantum Mater.* **5**, 59 (2020).
55. Zhou, T., Gao, Y. & Wang, Z. Spin excitations in nickelate superconductors. *Sci. China Phys. Mech. Astron.* **63**, 1–9 (2020).
56. Lechermann, F. Multiorbital processes rule the Nd_{1-x}Sr_xNiO₂ normal state. *Phys. Rev. X* **10**, 041002 (2020).
57. Lane, C. et al. Antiferromagnetic ground state of La₂CuO₄: a parameter-free ab initio description. *Phys. Rev. B* **98**, 125140 (2018).
58. Lane, C. & Zhu, J.-X. Identifying topological superconductivity in two-dimensional transition-metal dichalcogenides. *Phys. Rev. Mater.* **6**, 094001 (2022).
59. Van Hove, L. The occurrence of singularities in the elastic frequency distribution of a crystal. *Phys. Rev.* **89**, 1189 (1953).
60. Irkhin, V. Y., Katanin, A. & Katsnelson, M. Effects of van Hove singularities on magnetism and superconductivity in the $t - t'$ Hubbard model: a parquet approach. *Phys. Rev. B* **64**, 165107 (2001).
61. Schulz, H. Superconductivity and antiferromagnetism in the two-dimensional Hubbard model: scaling theory. *Europhys. Lett.* **4**, 609 (1987).
62. Markiewicz, R. A survey of the van Hove scenario for high-*t_c* superconductivity with special emphasis on pseudogaps and striped phases. *J. Phys. Chem. Solids* **58**, 1179–1310 (1997).
63. Bok, J. & Bouvier, J. Superconductivity and the Van Hove scenario. *J. Superconduct. Nov. Magn.* **25**, 657–667 (2012).
64. Newns, D., Krishnamurthy, H., Pattnaik, P., Tsuei, C. & Kane, C. Saddle-point pairing: an electronic mechanism for superconductivity. *Phys. Rev. Lett.* **69**, 1264 (1992).
65. Zheleznyak, A. T., Yakovenko, V. M. & Dzyaloshinskii, I. E. Parquet solution for a flat fermi surface. *Phys. Rev. B* **55**, 3200 (1997).
66. Zanchi, D. & Schulz, H. Weakly correlated electrons on a square lattice: a renormalization group theory. *Europhys. Lett.* **44**, 235 (1998).
67. Moriya, T. *Spin Fluctuations in Itinerant Electron Magnetism*, vol. 56 (Springer Science & Business Media, 2012).
68. Tremblay, A.-M. S. Two-particle-self-consistent approach for the Hubbard model. in *Strongly Correlated Systems*, 409–453 (Springer, 2012).
69. Sun, W. et al. Evidence for quasi-two-dimensional superconductivity in infinite-layer nickelates. Preprint at arXiv <https://doi.org/10.48550/arXiv.2204.13264> (2022).
70. Lu, H. et al. Magnetic excitations in infinite-layer nickelates. *Science* **373**, 213–216 (2021).
71. Igarashi, J.-i & Fulde, P. Spin waves in a doped antiferromagnet. *Phys. Rev. B* **45**, 12357 (1992).
72. Das, T., Markiewicz, R. & Bansil, A. Intermediate coupling model of the cuprates. *Adv. Phys.* **63**, 151–266 (2014).
73. Meyers, D. et al. Doping dependence of the magnetic excitations in La_{2-x}Sr_xCuO₄. *Phys. Rev. B* **95**, 075139 (2017).
74. Zhou, K.-J. et al. Persistent high-energy spin excitations in iron-pnictide superconductors. *Nat. Commun.* **4**, 1470 (2013).
75. Kaneshita, E., Tsutsui, K. & Tohyama, T. Spin and orbital characters of excitations in iron arsenide superconductors revealed by simulated resonant inelastic X-ray scattering. *Phys. Rev. B* **84**, 020511 (2011).
76. Peng, Y. et al. Influence of apical oxygen on the extent of in-plane exchange interaction in cuprate superconductors. *Nat. Phys.* **13**, 1201–1206 (2017).
77. Kastner, M., Birgeneau, R., Shirane, G. & Endoh, Y. Magnetic, transport, and optical properties of monolayer copper oxides. *Rev. Mod. Phys.* **70**, 897 (1998).
78. Sun, J. et al. Accurate first-principles structures and energies of diversely bonded systems from an efficient density functional. *Nat. Chem.* **8**, 831–836 (2016).
79. Pokharel, K. et al. Sensitivity of the electronic and magnetic structures of cuprate superconductors to density functional approximations. *npj Comput. Mater.* **8**, 31 (2022).
80. Leonov, I. Effect of lattice strain on the electronic structure and magnetic correlations in infinite-layer (Nd,Sr)NiO₂. *J. Alloy. Compd.* **883**, 160888 (2021).
81. Choi, M.-Y., Pickett, W. E. & Lee, K.-W. Fluctuation-frustrated flat band instabilities in ndnio₂. *Phys. Rev. Res.* **2**, 033445 (2020).
82. Chen, H., Hampel, A., Karp, J., Lechermann, F. & Millis, A. J. Dynamical mean field studies of infinite layer nickelates: physics results and methodological implications. *Front. Phys.* **10**, 16 (2022).
83. Wang, Z., Zhao, X.-G., Koch, R., Billinge, S. J. & Zunger, A. Understanding electronic peculiarities in tetragonal FeSe as local structural symmetry breaking. *Phys. Rev. B* **102**, 235121 (2020).
84. Kreisel, A., Andersen, B. M., Rømer, A. T., Eremin, I. M. & Lechermann, F. Superconducting instabilities in strongly correlated infinite-layer nickelates. *Phys. Rev. Lett.* **129**, 077002 (2022).
85. Zunger, A., Wei, S.-H., Ferreira, L. & Bernard, J. E. Special quasirandom structures. *Phys. Rev. Lett.* **65**, 353 (1990).
86. Kitatani, M. et al. Optimizing superconductivity: from cuprates via nickelates to palladates. *Phys. Rev. Lett.* **130**, 166002 (2023).
87. Hu, L.-H. & Wu, C. Two-band model for magnetism and superconductivity in nickelates. *Phys. Rev. Res.* **1**, 032046 (2019).
88. Kang, C.-J. & Kotliar, G. Optical properties of the infinite-layer La_{1-x}Sr_xNiO₂ and hidden Hund's physics. *Phys. Rev. Lett.* **126**, 127401 (2021).
89. Zhang, Y.-H. & Vishwanath, A. Type-II t-j model in superconducting nickelate Nd_{1-x}Sr_xNiO₂. *Phys. Rev. Res.* **2**, 023112 (2020).
90. Werner, P. & Hoshino, S. Nickelate superconductors: multiorbital nature and spin freezing. *Phys. Rev. B* **101**, 041104 (2020).
91. Plienbunrung, T., Daghofer, M., Schmid, M. & Oleś, A. M. Screening in a two-band model for superconducting infinite-layer nickelate. *Phys. Rev. B* **106**, 134504 (2022).
92. Been, E. et al. Electronic structure trends across the rare-earth series in superconducting infinite-layer nickelates. *Phys. Rev. X* **11**, 011050 (2021).
93. Hirayama, M., Nomura, Y. & Arita, R. Ab initio downfolding based on the gw approximation for infinite-layer nickelates. *Front. Phys.* **10**, 824144 (2022).
94. Wu, X. et al. Robust d_{x²-y²}-wave superconductivity of infinite-layer nickelates. *Phys. Rev. B* **101**, 060504 (2020).
95. Nomura, Y. et al. Formation of a two-dimensional single-component correlated electron system and band engineering in the nickelate superconductor ndnio₂. *Phys. Rev. B* **100**, 205138 (2019).
96. Gao, J., Peng, S., Wang, Z., Fang, C. & Weng, H. Electronic structures and topological properties in nickelates Ln_{n+1}Ni_nO_{2n+2}. *Natl. Sci. Rev.* **8**, nwa218 (2021).
97. Zhang, Y. et al. Competing stripe and magnetic phases in the cuprates from first principles. *Proc. Natl. Acad. Sci. USA* **117**, 68–72 (2020).
98. Kresse, G. & Joubert, D. From ultrasoft pseudopotentials to the projector augmented-wave method. *Phys. Rev. B* **59**, 1758–1775 (1999).
99. Kresse, G. & Furthmüller, J. Efficient iterative schemes for ab initio total-energy calculations using a plane-wave basis set. *Phys. Rev. B* **54**, 11169–11186 (1996).
100. Kresse, G. & Hafner, J. Ab initio molecular dynamics for open-shell transition metals. *Phys. Rev. B* **48**, 13115–13118 (1993).
101. Sun, J., Ruzsinszky, A. & Perdew, J. Strongly constrained and appropriately normed semilocal density functional. *Phys. Rev. Lett.* **115**, 036402 (2015).
102. Pizzi, G. et al. Wannier90 as a community code: new features and applications. *J. Phys. Condens. Matter* **32**, 165902 (2020).
103. Marzari, N., Mostofi, A. A., Yates, J. R., Souza, I. & Vanderbilt, D. Maximally localized Wannier functions: theory and applications. *Rev. Mod. Phys.* **84**, 1419 (2012).
104. Miyake, T. & Aryasetiawan, F. Efficient algorithm for calculating noninteracting frequency-dependent linear response functions. *Phys. Rev. B* **61**, 1712 (2000).
105. Shishkin, M. & Kresse, G. Implementation and performance of the frequency-dependent gw method within the paw framework. *Phys. Rev. B* **74**, 035101 (2006).

Acknowledgements

The authors would like to thank Dr. Peter Mistark for many fruitful discussions. The work at Los Alamos National Laboratory was carried out under the auspices of the US Department of Energy (DOE) National Nuclear Security Administration under Contract No. 89233218CNA000001. It was supported by the LANL LDRD Program, the Quantum Science Center, a U.S. DOE Office of Science National Quantum Information Science Research Center, and in part by the Center for Integrated Nanotechnologies, a DOE BES user facility, in partnership with the LANL Institutional Computing Program for computational resources. Additional computations were performed at the National Energy Research Scientific Computing Center (NERSC), a U.S. Department of Energy Office of Science User Facility located at Lawrence Berkeley National Laboratory, operated under Contract No. DE-AC02-05CH11231 using NERSC award ERCAP0020494. The work at Tulane University was supported by the U.S. Office of Naval Research (ONR) Grant No. N00014-22-1-2673. The work at Tulane University was also supported by start-up funding from Tulane University, the Cypress Computational Cluster at Tulane, the Extreme Science and Engineering Discovery Environment (XSEDE), and the National Energy Research Scientific Computing Center. The work at Northeastern University was supported by the US Department of Energy, Office of Science, Basic Energy Sciences

Grant No. DE-SC0022216 and benefited from Northeastern University's Advanced Scientific Computation Center and the Discovery Cluster, and the National Energy Research Scientific Computing Center through DOE Grant No. DE-AC02-05CH11231. B.B. acknowledges support from the COST Action CA16218.

Author contributions

C.L. and R.Z. performed computations, and C.L., R.Z., B.B., R.S.M., and J.Z. analyzed the data. C.L., A.B., J.S., and J.Z. led the investigations, designed the computational approaches, provided computational infrastructure, and analyzed the results. All authors contributed to the writing of the paper.

Competing interests

The authors declare no competing interests.

Additional information

Supplementary information The online version contains supplementary material available at <https://doi.org/10.1038/s42005-023-01213-0>.

Correspondence and requests for materials should be addressed to Christopher Lane.

Peer review information *Communications Physics* thanks the anonymous reviewers for their contribution to the peer review of this work.

Reprints and permission information is available at <http://www.nature.com/reprints>

Publisher's note Springer Nature remains neutral with regard to jurisdictional claims in published maps and institutional affiliations.



Open Access This article is licensed under a Creative Commons Attribution 4.0 International License, which permits use, sharing, adaptation, distribution and reproduction in any medium or format, as long as you give appropriate credit to the original author(s) and the source, provide a link to the Creative Commons license, and indicate if changes were made. The images or other third party material in this article are included in the article's Creative Commons license, unless indicated otherwise in a credit line to the material. If material is not included in the article's Creative Commons license and your intended use is not permitted by statutory regulation or exceeds the permitted use, you will need to obtain permission directly from the copyright holder. To view a copy of this license, visit <http://creativecommons.org/licenses/by/4.0/>.

© The Author(s) 2023